

Controlling Liquid Crystal Orientations for Programmable Anisotropic Transformations in Cellular Microstructures

Shucong Li, Gabriele Librandi, Yuxing Yao, Austin J. Richard, Alyssa Schneider-Yamamura, Joanna Aizenberg,* and Katia Bertoldi*

Geometric reconfigurations in cellular structures have recently been exploited to realize adaptive materials with applications in mechanics, optics, and electronics. However, the achievable symmetry breakings and corresponding types of deformation and related functionalities have remained rather limited, mostly due to the fact that the macroscopic geometry of the structures is generally co-aligned with the molecular anisotropy of the constituent material. To address this limitation, cellular microstructures are fabricated out of liquid crystalline elastomers (LCEs) with an arbitrary, user-defined liquid crystal (LC) mesogen orientation encrypted by a weak magnetic field. This platform enables anisotropy to be programmed independently at the molecular and structural levels and the realization of unprecedented director-determined symmetry breakings in cellular materials, which are demonstrated by both finite element analyses and experiments. It is illustrated that the resulting mechanical reconfigurations can be harnessed to program microcellular materials with switchable and direction-dependent frictional properties and further exploit "area-specific" deformation patterns to locally modulate transmitted light and precisely guide object movement. As such, the work provides a clear route to decouple anisotropy at the materials level from the directionality of the macroscopic cellular structure, which may lead to a new generation of smart and adaptive materials and devices.

Significant geometric reconfigurations have recently been introduced by making cellular structures out of stimuli-responsive materials.^[11–14] Such symmetry breakings hold promise for the design of smart systems with highly tunable symmetry-dependent optical,^[15] frictional,^[16] wetting,^[17] as well as acoustic properties.^[18] However, the range of accessible deformations has mostly been limited to simple contraction/extension and/or bending of the constitutive plates and struts. To unlock more complex deformations at the plate level, sophisticated control over the constituent material anisotropy has to be achieved.

Liquid crystalline elastomers (LCEs) are a unique class of soft materials that combine the elasticity of an elastomer with the molecular anisotropy of the liquid crystalline phase (Figure 1A). Such intrinsic molecular anisotropy determined by the mesogenic alignment (referred to as mesogenic director, Figure 1A) enables programming of mechanical deformations through a nematic–isotropic (N–I) phase transition^[19,20] in response to various environmental stimuli (e.g., heat,^[19] light,^[21]

electric field,^[22] and magnetic field^[23,24]). To control the mesogenic alignment and therefore the type of achievable mechanical deformation and symmetry breaking, various methods have been proposed. Surface-based alignment, including photo-alignment^[25,26] and nano-/microgroove-based alignment,^[27,28] has allowed complex patterning of directors in space,^[25] but it is most effective in 2D thin film systems. As another route, mechanical shearing obtained either via mechanical stretching^[29] or 3D/4D printing^[30,31] has been used to fabricate LCE structures with more complex geometries; however, these approaches cannot decouple LCE anisotropy from structural architecture, since they limit the achievable mesogenic alignment only to the shearing direction. Finally, it has been shown that 3D LCE microstructures with arbitrary uniaxial mesogenic alignment can be obtained by applying a magnetic field during polymerization.^[32,33] This latter capability opens up the possibility to decouple the materials anisotropy at the molecular scale from the orientation of the cellular structure at the architectural scale, and realize mechanical transformations that are rarely achieved in cellular materials.

Here, we demonstrate that a palette of symmetry breakings can be realized in substrate-attached LCE cellular

1. Introduction

Cellular structures comprising networks of plates/struts connected to form arrays of polygons have attracted great attention because of their remarkable geometry-determined functionalities.^[1] These include exotic properties such as negative Poisson's ratio,^[2] negative swelling,^[3] negative refractive indices,^[4,5] as well as high strength-to-weight ratio^[6–9] and energy absorption.^[10]

S. Li, Y. Yao, J. Aizenberg
Department of Chemistry and Chemical Biology
Harvard University
Cambridge, MA 02138, USA
E-mail: jaiz@seas.harvard.edu

G. Librandi, A. J. Richard, A. Schneider-Yamamura, J. Aizenberg,
K. Bertoldi
Harvard John A. Paulson School of Engineering and Applied Sciences
Harvard University
Cambridge, MA 02138, USA
E-mail: bertoldi@seas.harvard.edu

 The ORCID identification number(s) for the author(s) of this article can be found under <https://doi.org/10.1002/adma.202105024>.

DOI: 10.1002/adma.202105024

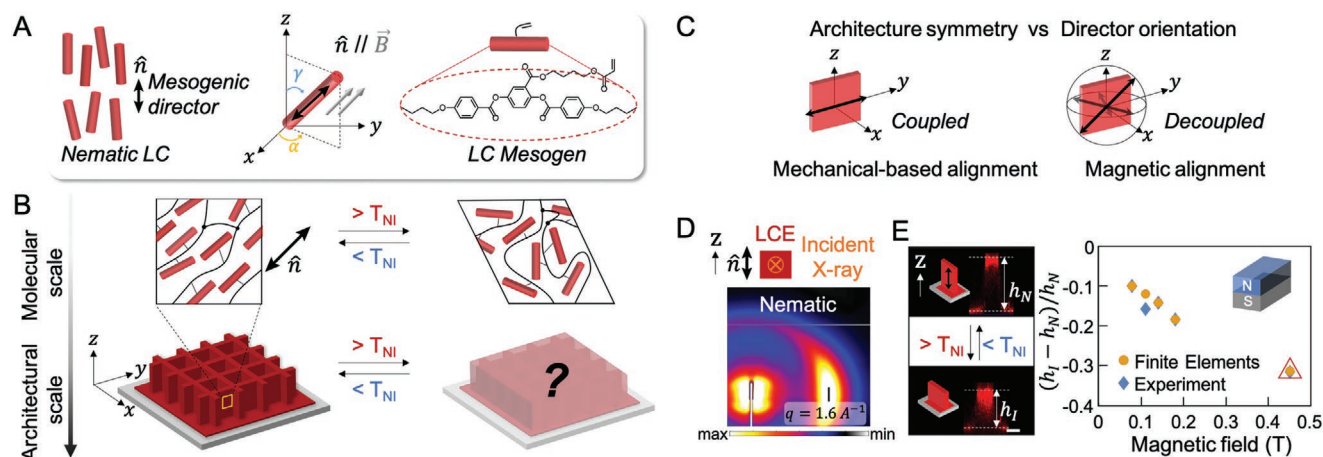


Figure 1. LCE cellular microstructures with decoupled molecular and architectural anisotropy and effect of the magnetic field on the LCE response. A) We use the azimuthal angle α and polar angle γ to denote the mesogenic director of the nematic liquid crystal. Molecular structure of the polymerizable liquid crystalline mesogen is shown on the right. B) The design principle to achieve a palette of symmetry breakings of the LCE cellular structures by independently programming anisotropy at the molecular and architectural scales. C) Mechanical-based alignment (left) does not allow decoupling of LCE anisotropy from structural architecture, as the molecular alignment always follows the stretching direction. By contrast, magnetic alignment (right) permits such decoupling by orienting the object in an arbitrary direction in the magnetic field. D) WAXS patterns of a z-aligned LCE block. Note that the incident X-ray is perpendicular to the mesogenic director. E) Left: Fluorescence confocal microscopy images of a z-aligned microplate at $T = 25\text{ }^\circ\text{C} < T_{\text{NI}}$ (top) and at $T = 135\text{ }^\circ\text{C} > T_{\text{NI}}$ (bottom). h_N and h_I denote the height of the plate in the nematic and isotropic phases, respectively. Right: Evolution of the temperature-responsive strain along the molecular director as a function of the strength of the applied magnetic field in LCE fabrication. The diamond and circular markers correspond to experimental data and FE predictions, respectively. The red triangular marker indicates the magnetic field (0.45 T) used in this study for all considered cellular structures.

microstructures by independently programming the anisotropy at the molecular and structural scales (Figure 1B,C). Specifically, we use magnetic field to realize an arbitrary uniaxial mesogenic alignment in the LCE material and study its effect on the deformation modes of microcellular structures with different architectural symmetries. Guided by a systematic understanding of the effect of the magnetic field on the mesogen orientation and the resulting LCE response, as well as Finite Element (FE) simulations, we first consider the vast design space and identify combinations of mesogenic director orientation, lattice symmetry, and lattice connectivity that lead to unexplored pattern transformations, including isotropic/anisotropic buckling, chiral/achiral buckling, tilting, twisting, and shearing. We then demonstrate that such deliberate symmetry breakings can be utilized to program direction-dependent and switchable frictional properties of cellular materials. We further demonstrate the capability to pattern region-specific and gradient director orientations in LCE microcellular surfaces, and exploit the resulting local deformation patterns to realize transmitted light modulation and controlled on-surface object transport. As such, our work provides not only insights in controlling the symmetry breaking in cellular structures, but also a promising platform for the design of the next generation of materials and devices with tunable direction-dependent properties and new functionalities.

2. Results and Discussion

Our LCE microstructures were fabricated out of a monomer mixture consisting of LC mesogens crosslinked with 7.5 wt% of 1,6-hexanediol diacrylate (Figures S1–S3, Supporting

Information). We first poured the LC mixture in a negative poly(dimethylsiloxane) (PDMS) mold of the desired microstructure and covered it with a glass substrate (Figures S4 and S5 and Table S1, Supporting Information). We then heated the LC mixture up to $T = 90\text{ }^\circ\text{C}$ to reach its isotropic phase (Figure S3, Supporting Information). Next, we take advantage of the anisotropic magnetic susceptibility of LC monomers of the mixture^[34] and use an external magnetic field to align the nematic directors. Specifically, guided by numerical simulations, we positioned the mold in the desired orientation within the magnetic field generated by commercially available magnets to realize an arbitrary, user-defined mesogenic alignment within the cellular microstructures. We then cooled down the unpolymerized mixture with aligned mesogens to its nematic phase (at $T = 60\text{ }^\circ\text{C}$) and subjected it to UV-polymerization under a nitrogen atmosphere for 30 min.^[33] Finally, we cooled down the sample to room temperature, and carefully peeled off the PDMS mold to release the surface-attached LCE microstructure (see Section S1.3.1, Supporting Information for additional details).

To quantify the resulting alignment of mesogens within the cellular structure, we conducted wide-angle X-ray scattering (WAXS) experiments (Figure 1D; Section S1.3.3, Supporting Information). We find that at $T = 60\text{ }^\circ\text{C}$ the scattering from LCE block exhibits a direction-dependent intensity profile with a distinct peak along the equatorial direction at $q = 1.6\text{ } \text{\AA}^{-1}$, which corresponds to the distance between neighboring mesogens.^[29] Based on these WAXS results, we can estimate the scalar order parameter in the nematic phase to be ≈ 0.21 (details in Section S1.3.3 and Figure S6, Supporting Information).^[35] Hence, using this strategy we can encrypt a user-defined mesogenic alignment to LCE structures with heights up to 1 mm, a size

range that represents a challenge for surface-based alignment methods, which often align micrometer-thick thin films.^[25–28]

While the mesogenic alignment is permanently encoded into LCE after polymerization process, the material undergoes nematic–isotropic transition when heated above its N–I phase transition temperature, $T_{NI} = 125\text{ }^{\circ}\text{C}$ (Figure S3B, Supporting Information), leading to a reversible, temperature-responsive mechanical actuation (note that the glass transition temperature for our LCEs is $T_g = 48\text{ }^{\circ}\text{C}$, Figure S3B, Supporting Information). As shown in Figure 1E, a surface-attached LCE microplate with size $250 \times 50 \times 200\text{ }\mu\text{m}$ (length \times width \times height) synthesized in a low-intensity magnetic field (0.45 T) aligned along its height shortens by $\varepsilon_z = (h_I - h_N)/h_N = -0.32$ (h_N and h_I denoting its height in the nematic and isotropic phases, respectively) upon N–I phase transition, regardless of the temperature ramping rate (see Figure S7, Supporting Information). Importantly, the extent of such deformation can be controlled by varying the intensity of the magnetic field applied during the polymerization process. In particular, we find that ε_z monotonically increases with the intensity of the magnetic field as a stronger magnetic field applied to the unpolymerized mixture leads to a higher scalar order parameter, see Figure 1E and Figure S8, Supporting Information.

While previous studies have investigated the deformation of either cellular structures with the nematic director aligned along the plates^[31] or simple shapes with an arbitrary nematic director,^[33,36] the interplay between LCE molecular anisotropy and the constraints introduced by the interconnectivity typical of cellular structures can largely expand the range of achievable deformations. To first explore how LCE molecular anisotropy can affect the deformation and symmetry breaking of surface-attached cellular structures, we conducted finite element (FE) simulations using the commercial package ABAQUS 2018/Standard. In all our numerical analyses, we discretized the models with 8-node linear brick solid elements (Figure S9, Supporting Information), and captured the response of LCEs using the strain energy density^[37]

$$W = \frac{1}{2} \left[\frac{E}{(1+\nu)(1-2\nu)} \delta_{ij} \delta_{kl} + \frac{E}{1+2\nu} (\delta_{ik} \delta_{jl} + \delta_{il} \delta_{jk}) \right] \varepsilon_{ij} \varepsilon_{kl} - \frac{\beta}{2} (S^t - S^0) (3n_i n_j - \delta_{ij}) \varepsilon_{ij} \quad (1)$$

where ε_{ij} is the Lagrange strain tensor, δ_{ij} is the Kronecker delta and $E = 0.4\text{ MPa}$ and $\nu = 0.49$ are the Young's modulus and Poisson's ratio of the LCE, respectively.^[38] Further, n_i is the i -th nematic director component, $S^0 = 0.21$ denotes the initial nematic scalar order parameter and S^t represents the instantaneous nematic scalar order parameter. Finally, β is a parameter defining the degree of coupling between the elastic strain energy and the potential energy introduced by the nematic order, which we set equal to 0.041 MPa as this value enables us to capture the experimental results reported in Figure 1E. In all our simulations, we assumed perfect bonding between the LCE cellular structures and the substrate and monotonically decreased S^t from S^0 to 0 to simulate the mechanical deformations arising from the loss of mesogen alignment occurring upon nematic–isotropic phase transition (see Supporting Information Section S2 for details).

To begin with, we focused on a surface-attached square lattice with $P4mm$ symmetry (Figure 2A and Figure S10, Supporting Information).^[39] We chose plates with $l/h = 0.6$ and $h/t = 6.67$, where l , h , and t denote the length, height and thickness of the plates, respectively, and used FE simulations to systematically explore how molecular anisotropy (i.e., the mesogenic director described by the azimuthal angle α and polar angle γ —Figure 1A) affects their meso-scale deformations. We find that four distinct, elementary deformation modes of cellular microstructures emerge when the nematic–isotropic phase transition of the LCE happens (Figure 2B–E). First, when the mesogenic director is along the C_4 rotational axis (i.e., $\alpha = 0^\circ$ and $\gamma = 0^\circ$), all plates in the isolated state expand in the x – y plane and shrink along the z axis (Figure 2B-top). While this plate deformation in an isolated square cell leads to a global expansion in the x – y plane (see Figure S11, Supporting Information), it is prevented by the neighbors in the interconnected square lattice. As such, each plate buckles into a half sinusoidal wave and leads to the formation of a wavy pattern with $P4gm$ symmetry (Figure 2B-center), similar to that previously observed for swollen square lattices made of isotropic materials.^[13] Second, when the mesogenic director is in the σ_{v1} mirror plane but tilted 45° away from C_4 axis (i.e., $\alpha = 0^\circ$ and $\gamma = 45^\circ$), both the horizontal and vertical plates undergo shearing in the same x – z plane (Figure 2C-top)—a deformation mode that is rarely encountered in microplates and stems from the molecular anisotropy of the constituent LCEs. Since the shearing direction and extent of each plate are compatible with that of the neighbors, similarly to the case of an isolated square cell (see Figure S11, Supporting Information), a rarely encountered global shearing of the interconnected lattice with a symmetry reduction to Pm is observed (i.e., only the mirror planes σ_{v1} and σ'_{v1} are preserved from the initial lattice—Figure 2C-center and Figure S11, Supporting Information). Third, when the nematic director is orthogonal to C_4 axis and in the σ_{v1} mirror plane (i.e., $\alpha = 0^\circ$ and $\gamma = 90^\circ$) the horizontal plates shrink along the x -axis while the vertical ones expand along the y -axis (Figure 2D-top), so that an isolated square cell transforms into a rectangular one (Figure S11, Supporting Information). However, as observed for $\alpha = 0^\circ$ and $\gamma = 0^\circ$, for the cellular structure the expansion of the vertical elements also results in buckling. Differently, the shrinkage of the horizontal plates is prevented by the neighboring elements and results in a tensile state of stress. This behavior leads to an anisotropic buckling pattern with Pm symmetry (Figure 2D-center). Fourth, when the mesogenic director is in the σ_{d1} mirror plane and orthogonal to C_4 axis (i.e., $\alpha = 45^\circ$ and $\gamma = 90^\circ$), all plates twist (Figure 2E-top and Figure S11, Supporting Information), resulting in a diamond-like pattern with $C2mm$ point group (Figure 2E-center). Finally, we want to emphasize the deformation shown in Figure 2B–E present four elementary modes, but many more symmetry breaking patterns can be achieved by systematically varying the mesogenic director's orientation (arbitrary angles α and γ) in 3D (Figure S10, Supporting Information). These additional actuation behaviors can be expressed as a combination of the four elementary deformation modes reported in Figure 2. For example, if the nematic director lies in the σ_{v1} mirror plane and is tilted by 22.5° away from C_4 axis (i.e., $\alpha = 0^\circ$ and $\gamma = 22.5^\circ$) a buckling instability mixed with a shearing deformation is expected to

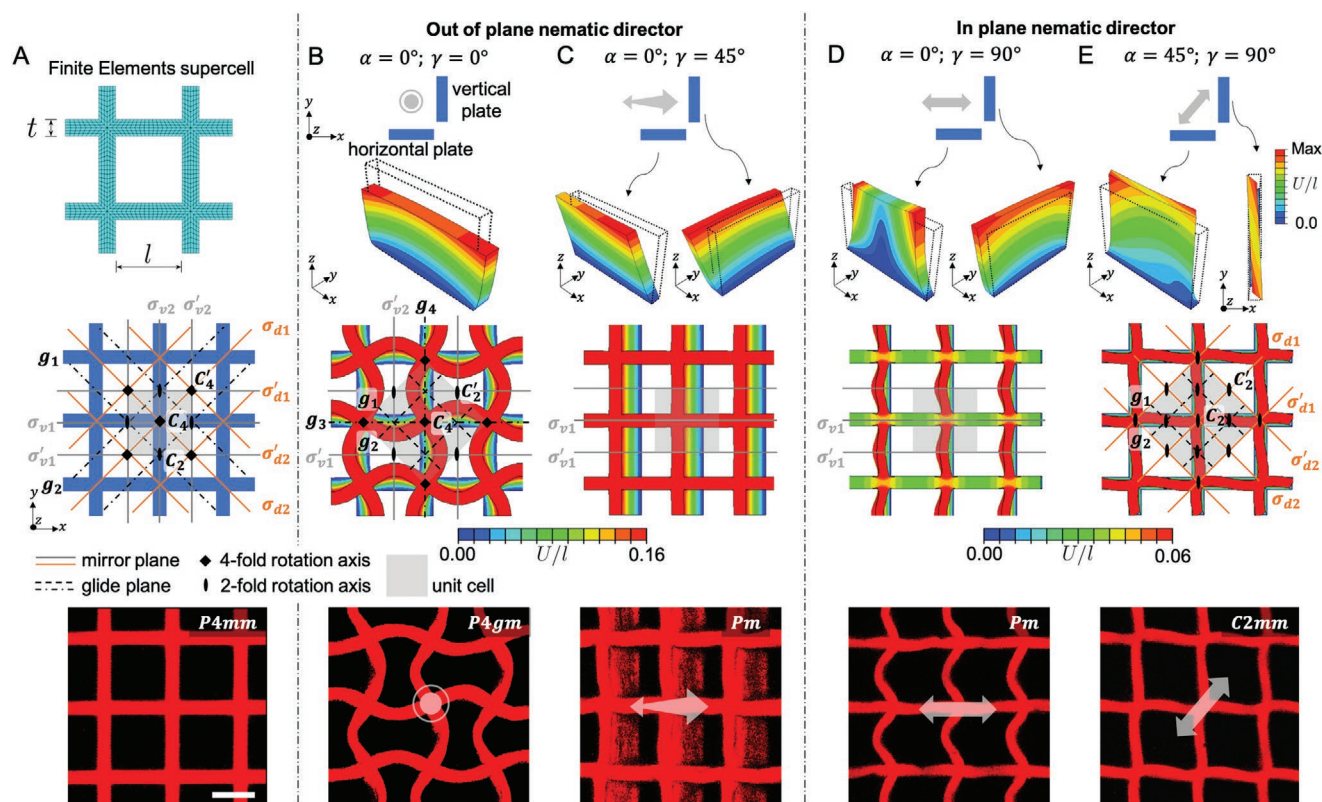


Figure 2. Symmetry breakings for a surface-attached LCE square microlattice. A) Top: FE supercell for deformation calculation. Center: lattice with $l/h = 0.6$ and $h/t = 6.67$ below T_{NI} with symmetric elements marked. Bottom: an experimental confocal microscopy image of undeformed LCE square microlattice. B–E) Deformed lattice above T_{NI} for the case of mesogenic alignment defined by: B) $\alpha = 0^\circ$, $\gamma = 0^\circ$; C) $\alpha = 0^\circ$, $\gamma = 45^\circ$; D) $\alpha = 0^\circ$, $\gamma = 90^\circ$; E) $\alpha = 45^\circ$, $\gamma = 90^\circ$. Top: FE results for isolated LCE microplates above T_{NI} . Center: FE results for an infinitely large square lattice upon N–I phase transition. Bottom: fluorescence confocal microscopy images showing the deformations of the microstructures at $T = 135^\circ\text{C} > T_{NI}$. For the FE results, we also show the normalized magnitude of the displacement field in the isotropic phase (displacement U divided by original lattice length l) in different colors. Double-headed gray arrows in the top and bottom row illustrate the projection of the 3D mesogenic director in the xy -plane. Note, the red color of the experimental results comes from the Rhodamine dye on LCE samples and does not reflect the deformation extent as shown in the FE analysis. Scale bar: $50\ \mu\text{m}$.

occur, whereas for $\alpha = 22.5^\circ$ and $\gamma = 90^\circ$ the lattice will anisotropically twist upon the N–I phase transition (Figure S10, Supporting Information).

To validate the numerical results, we fabricated a square lattice identical to that investigated in Figure 2 with $l = 60\ \mu\text{m}$, $t = 15\ \mu\text{m}$, and $h = 100\ \mu\text{m}$ with the method described above (see Section S1.3, Supporting Information for details). Remarkably, for all considered mesogenic directors the samples deformed as predicted by the FE simulations (Figure 2—bottom; Figure S12, Movie S1, and Movie S2, Supporting Information), confirming that the molecular anisotropy encrypted in the LCE relative to the orientation of the structure at the architectural scale can be exploited to program a wide range of deformations and symmetry breaking in microcellular structures. However, while in the FE analysis we apply an infinitesimal perturbation to guide the formation of a single buckling phase, in our experiments multiple (right- and left-handed) buckling phases emerge triggered by several nucleation events (Figure S13, Supporting Information). Finally, we note the bonding between the LCE cellular structures and the substrate significantly affects their deformation behavior, as in the presence of low interfacial adhesion no buckling is observed (Figure S14, Supporting Information).

We next use FE simulations to investigate the response of architectures with different symmetries. Focusing on a $P6mm$ triangular lattice structure with $l/h = 1.9$ and $h/t = 4.27$, we find that, when the nematic director is aligned along the z -axis (i.e., $\alpha = 0^\circ$ and $\gamma = 0^\circ$), each plate buckles into a full sinusoidal wave (Figure 3A and Movie S2, Supporting Information), resulting in the formation of a chiral pattern.^[13] Interestingly, when the nematic director is oriented along the x -axis (i.e., $\alpha = 0^\circ$ and $\gamma = 90^\circ$), the two oblique edges of each triangle twist by the same amount but in the opposite directions, while the horizontal edge does not deform significantly, remaining in a tensile state of stress. The latter deformations lead to an achiral hourglass-like pattern not observed in previously reported cellular structures, with a mirror plane σ_v cutting through the nodes (Figure 3B and Movie S2, Supporting Information). Note that in this pattern the angles between neighboring plates at the joints are not preserved, an unusual feature which stems from the molecular anisotropy. Further, more unusual symmetry breakings can be achieved by combining this symmetric twisting with other elementary deformations through the control of the director orientation in the LCE material (Figure S15, Supporting Information).

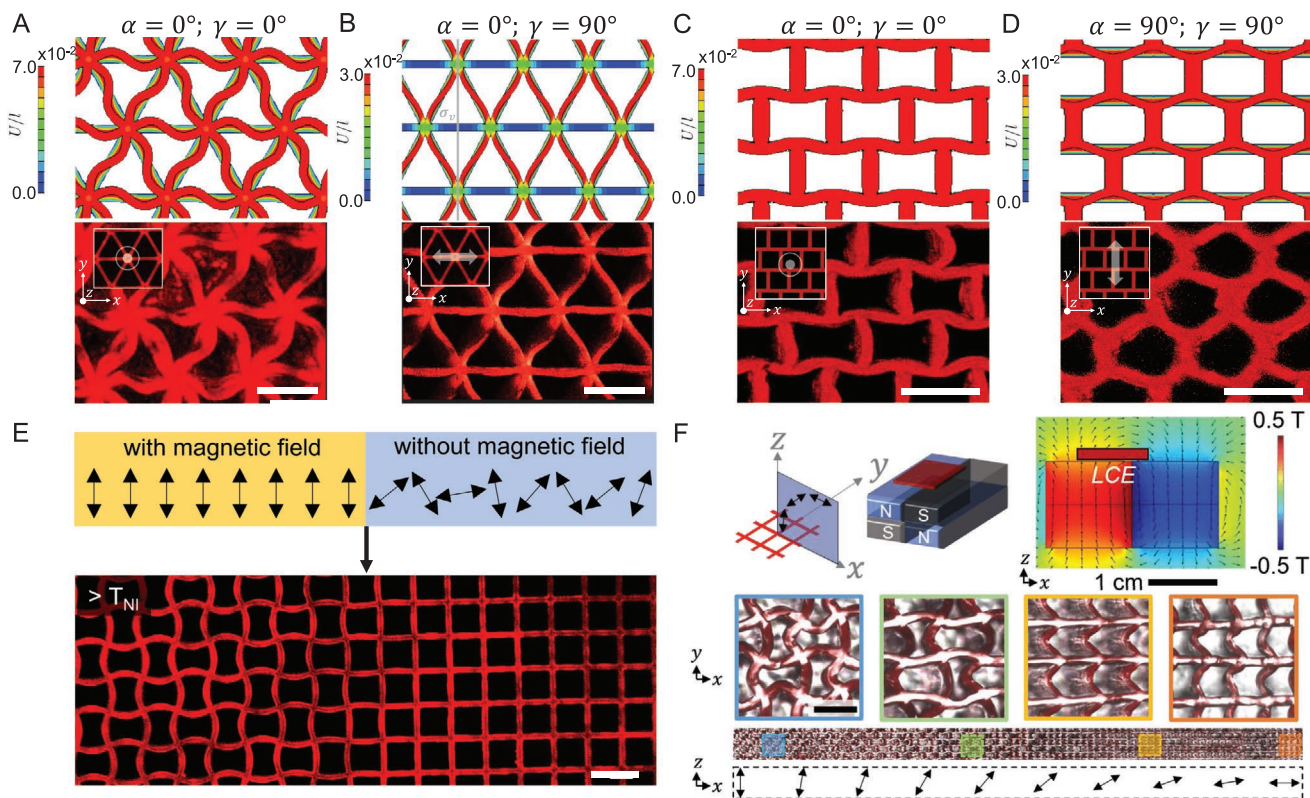


Figure 3. Introduction of different lattice geometries and area-specific director orientations to LCE microcellular structures. A–D) FE simulations for infinitely large lattices (top) and fluorescence confocal microscopy images (bottom) depicting the deformations of the lattices above T_{NI} for: A) triangular lattice with $l/h = 1.9$ and $h/t = 4.27$ above T_{NI} for the case of mesogenic alignment with $\alpha = 0^\circ$, $\gamma = 0^\circ$; B) triangular lattice with the mesogenic alignment defined by $\alpha = 0^\circ$, $\gamma = 90^\circ$; C) staggered square lattice with $l/h = 0.6$ and $h/t = 6.67$ above T_{NI} for the case of mesogenic alignment with $\alpha = 0^\circ$, $\gamma = 0^\circ$; D) staggered square lattice with mesogenic alignment defined by $\alpha = 90^\circ$, $\gamma = 90^\circ$. The color in FE results corresponds to the normalized magnitude of the displacement field in the isotropic phase (displacement U divided by original lattice length l). Fluorescence confocal microscopy images illustrate the deformations of the microstructures at $T = 135^\circ\text{C} > T_{NI}$. The insets in the top left corner of the microscopy images show the structure of the undeformed lattice below T_{NI} . The double-headed gray arrows in the inset illustrate the projection of the 3D mesogenic director in the xy -plane. E) Experimental fluorescence confocal microscopy image of an LCE square lattice strip with $l/h = 0.6$, $h/t = 6.67$, and $h = 100\ \mu\text{m}$ at $T = 135^\circ\text{C} > T_{NI}$. Stepwise polymerization has been used to introduce z -alignment on the left and isotropic alignment on the right. Schematics of the mesogenic director are shown on the top. F) Top: a magnetic field with orientation continuously changing from z -axis to x -axis can be generated by placing two magnets side-by-side with N poles facing upward and downward, respectively. The right plot shows the resulting magnetic field calculated using COMSOL. Bottom: optical microscopy images of an LCE square lattice polymerized in such spatially varying magnetic field. At $T = 135^\circ\text{C} > T_{NI}$ the lattice displays gradually changing, region-specific symmetry breakings along the strip. The double-headed arrows in (E) and (F) mark the mesogenic director. Scale bars: A–F) $100\ \mu\text{m}$.

While so far we have focused on cellular structures with edges connected end-to-end with a center of inversion symmetry i at the nodes, we next consider a staggered brick-wall architecture with $C2mm$ symmetry and edges connected in an end-to-side manner to provide enhanced flexibility at the nodes. This geometry transforms into a re-entrant hexagonal lattice when the nematic director is aligned along the z -axis (i.e., $\alpha = 0^\circ$ and $\gamma = 0^\circ$, Figure 3C) and into a pseudo-hexagonal lattice when the nematic director is along the y -axis (i.e., $\alpha = 90^\circ$ and $\gamma = 90^\circ$, Figure 3D), with $C2mm$ symmetry preserved in both cases. It is important to highlight that these lattice transformations are not triggered by any buckling instabilities, which are prevented by the enhanced flexibility of the nodes. As such, these results indicate that the range of achievable deformations can be further expanded by engineering the nodes to control the lattice connectivity (Figure S16, Supporting Information).

Further, our approach based on magnetic alignment enables us to expand the range of deformations by encoding area-specific mesogenic alignments in the LCEs to ultimately realize spatially varying deformation modes. For example, utilizing stepwise polymerization with a photomask, we can readily prescribe director alignment only to certain regions where anisotropic deformation will take place locally (Figure 3E). Additionally, more control on the local mesogenic alignment can be achieved by applying a spatially varying magnetic field. As an example, a magnetic field with orientation continuously changing from z -axis to x -axis can be generated by placing two magnets side-by-side with N poles facing upward and downward, respectively (Figure 3F; Figures S17 and S18, Supporting Information). Importantly, by applying such a magnetic field during the polymerization process, a gradient of the director orientations along the sample can be encoded. As shown in Figure 3F, when applied to a square lattice, the buckled pattern

with $P4gm$ symmetry shown in Figure 2B emerges on the left side in the isotropic phase and the anisotropic buckling pattern with Pm symmetry reported in Figure 2D on the right side, whereas in between the deformation seamlessly evolve between these two distinct symmetry states (see Figures S17 and S18, Supporting Information for the results in a triangular lattice).

Having demonstrated that the interplay between molecular and architectural anisotropy in cellular structures gives rise to a wide range of deformations, we now explore the possibility to engineer LCE microcellular surfaces with switchable and direction-dependent properties induced by designed symmetry breakings. Since the high strength/weight ratio of cellular structures makes our surfaces a good candidate for object transportation (note that they can hold objects $\approx 100\times$ heavier than themselves), we consider a square lattice with different mesogenic alignments and study the effect of the triggered symmetry breakings on its surface frictional properties. In our tests, we heated the LCE samples up to $T = 135^\circ\text{C} > T_{NI}$ (a temperature well above T_g), placed a metal ball (diameter

5 mm, weight 0.5 g, $\approx 100\times$ heavier than the weight of LCE cellular structures underneath) on their surface, slowly tilted the underlying stage and measured the smallest tilting angle, θ_{cr} , for which the metal ball started to roll (see Supporting Information for details). Note that we considered four different sliding directions: two parallel to the σ_{v1} mirror plane (identified by $\eta = 90^\circ$ and 270°) and two parallel to the σ_{v2} mirror plane (identified by $\eta = 0^\circ$ and 180°)—see inset in Figure 4A). In Figure 4A, we report θ_{cr} measured for the four sliding directions in the case of mesogenic director aligned (i) isotropically, (ii) along the z axis (i.e., $\alpha = 0^\circ$ and $\gamma = 0^\circ$), (iii) in the σ_{v1} mirror plane and tilted 45° from the C_4 axis (i.e., $\alpha = 0^\circ$ and $\gamma = 45^\circ$) and (iv) along the x axis (i.e., $\alpha = 0^\circ$ and $\gamma = 90^\circ$). As expected, in the case of isotropic alignment, θ_{cr} is identical in four considered sliding directions ($\theta_{cr} \approx 2.0^\circ$, see black dot in Figure 4A, left) as the lattice maintains the $P4mm$ symmetry upon heating above T_{NI} . Similar isotropic sliding behavior is observed also for $\alpha = 0^\circ$ and $\gamma = 0^\circ$, since the structure retains C_4 rotational symmetry through the N–I phase transition. However, for $\alpha = 0^\circ$

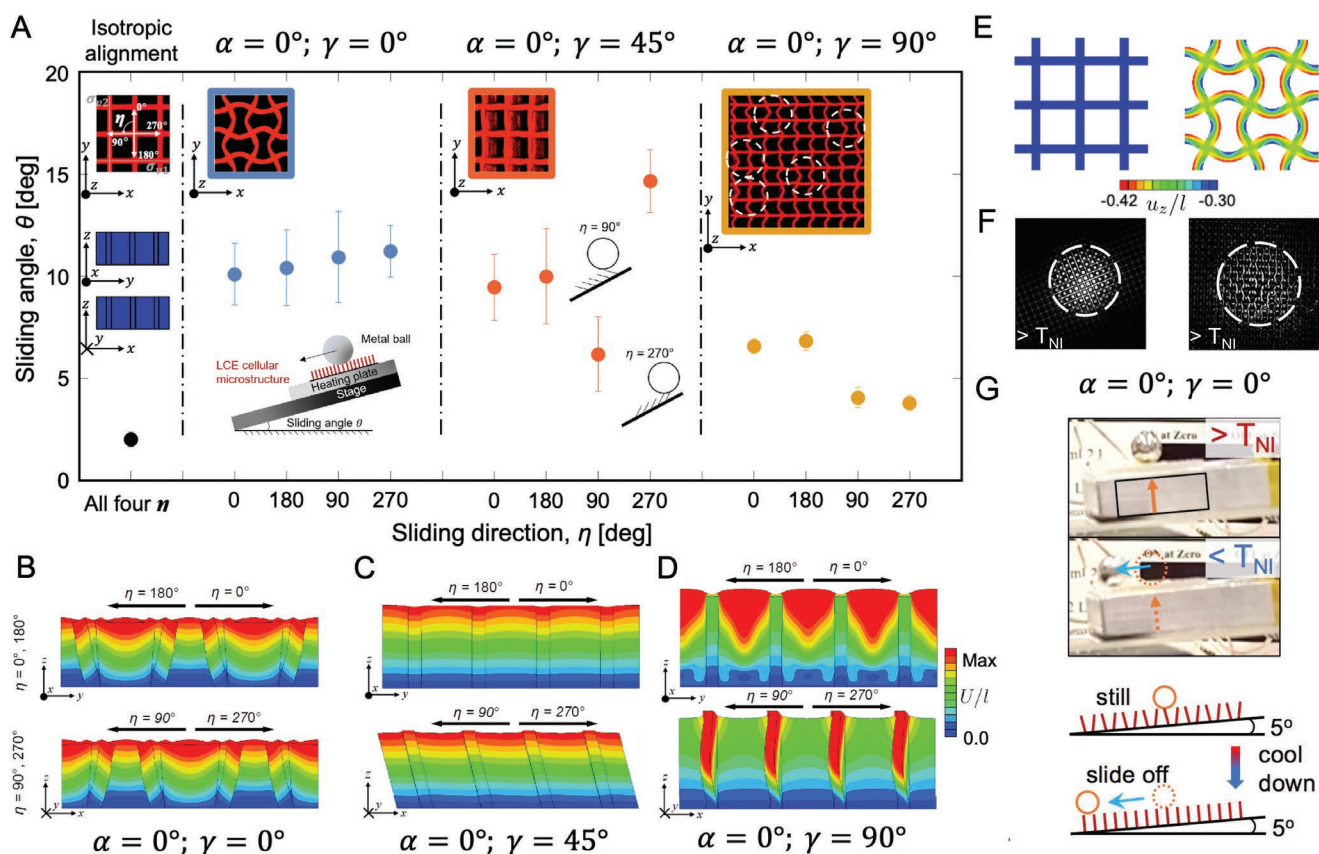


Figure 4. Direction-dependent and switchable frictional properties. A) Sliding angles of metal balls, θ_{cr} , along four orthogonal directions of an LCE square microcellular structures with $l/h = 0.6$ and $h/t = 6.67$ at $T = 135^\circ\text{C} > T_{NI}$ for isotropic alignment and mesogenic director defined by $(\alpha, \gamma) = (0^\circ, 0^\circ)$, $(0^\circ, 45^\circ)$ and $(0^\circ, 90^\circ)$. Insets show the fluorescence microscopy data for the corresponding symmetry breaking of the LCE microlattices and the experimental setup and anisotropy in wall orientation. Note that buckling of the walls in the case of $(\alpha, \gamma) = (0^\circ, 90^\circ)$ occurs in both right and left directions, as depicted by the circled regions in the microscopy image. B–D) FE snapshots showing side views (in both the yz - and xz -planes) of square lattices in the isotropic phase with mesogenic director defined by B) $(\alpha, \gamma) = (0^\circ, 0^\circ)$; C) $(0^\circ, 45^\circ)$; and D) $(0^\circ, 90^\circ)$. Color denotes the normalized amplitude of the displacement field. E) FE snapshots showing top views of square lattices in the isotropic phase for isotropic alignment and mesogenic director defined by $(\alpha, \gamma) = (0^\circ, 0^\circ)$. Color denotes the normalized amplitude of the displacement along the z direction. F) Microscopy images illustrating the contact area between the metal ball and the LCE cellular surface in the isotropic phase for isotropic alignment and mesogenic director defined by $(\alpha, \gamma) = (0^\circ, 0^\circ)$. G) For a square lattice with $\alpha = 0^\circ$ and $\gamma = 0^\circ$, a metal ball remains still for $T > T_{NI}$ and roll for $T < T_{NI}$ when $\theta = 5^\circ$.

and $\gamma = 0^\circ$, θ_{cr} is substantially larger than the one found for the isotropic lattice (i.e., 10.5° vs 2.0°), despite the similar elastic modulus of the two structures at high temperature. We attribute such difference to the non-planar features induced by buckling of the surface of the structure (Figure 4E) as well as a slight increase of the contact area between LCE and the metal ball (Figure 4F) for $\alpha = 0^\circ$ and $\gamma = 0^\circ$.

Differently, in the case of $(\alpha, \gamma) = (0, 45^\circ)$ and $(0, 90^\circ)$, θ_{cr} shows a pronounced direction-dependence, which is consistent with the Pm symmetry exhibited by these lattices in the isotropic phase. More specifically, in the case of $\alpha = 0^\circ$ and $\gamma = 45^\circ$, we find that $\theta_{cr} \approx 10.0^\circ$ for $\eta = 0^\circ$ and 180° , whereas $\theta_{cr} \approx 6.0^\circ$ and $\approx 15.0^\circ$ for $\eta = 90^\circ$ and 270° , respectively, with the difference in θ_{cr} measured for $\eta = 90^\circ$ and 270° caused by the sheared plates that facilitate the rolling along the shearing direction ($\eta = 90^\circ$), but provide additional resistance for rolling in the opposite direction ($\eta = 270^\circ$; see insets in Figure 4A and Figure 4C). Further, for $\alpha = 0^\circ$ and $\gamma = 90^\circ$, we find that $\theta_{cr} \approx 5.5^\circ$ for $\eta = 0^\circ, 180^\circ$ and $\theta_{cr} \approx 4.0^\circ$ for $\eta = 90^\circ, 270^\circ$. Although this mesogenic alignment also leads to a pattern with Pm symmetry in the isotropic LC phase, as suggested in Figure 2D, the lack of anisotropy along the x -axis caused by the buckling both leftwards and rightwards can introduce domain-like patterns (see rightmost inset in Figure 4A) and thus eliminating the difference between θ_{cr} for $\eta = 90^\circ$ and 270° . Moreover, we want to point out that the observed behaviors are robust, as the deterioration of the lattices upon multiple cycles of actuation is minimal (Figure S19, Supporting Information) and that the presence of metal ball does not affect the deformation behaviors of LCE structures (Figure S20, Supporting Information).

Remarkably, our platform not only allows for direction-dependent frictional properties, but also provides means to change these properties by programming the temperature. For example, since for a square lattice with $\alpha = 0^\circ$ and $\gamma = 0^\circ$, $\theta_{cr} \approx 2^\circ$ and $\approx 10^\circ$ at $T = 115^\circ\text{C}$ and $T = 135^\circ\text{C}$, respectively, we expect the metal ball to remain still for $T > T_{NI}$ and roll for $T < T_{NI}$ when $\theta \in [2^\circ, 10^\circ]$. The experimental results reported in Figure 4G for $\theta = 5^\circ$ at $T = 135^\circ\text{C}$ (above T_{NI} and T_g) and 115°C (below T_{NI} and above T_g) confirm our hypothesis and demonstrate that the sliding of the metal ball can be dynamically controlled by simply changing the temperature (see also Movie S3, Supporting Information). These results suggest the potential of our platform to dynamically control the adhesion force and movement on the objects sitting above.

The results of Figure 4 suggest that the designed symmetry breakings not only affect the direction-dependent frictional properties of the LCEs microcellular surfaces in the static regime, but also in the dynamic one, opening avenues for a new range of applications, such as locomotion and objects transport. To further demonstrate this point, we harness our capability to encode customizable area-specific director alignment to realize selective object transport. In particular, we consider a square lattice polymerized in a spatially varying magnetic field similar to the one shown in Figure 3F, so that the mesogen director gradually changes from $\gamma = 70^\circ$ to 110° , while keeping $\alpha = 0^\circ$. Such spatially varying nematic alignment induces the lattice walls to tilt towards the sample center upon thermal actuation (see schematics in Figure 5A and Figure S19C, Supporting Information). As such, while for $T = 110^\circ\text{C} < T_{NI}$, in full

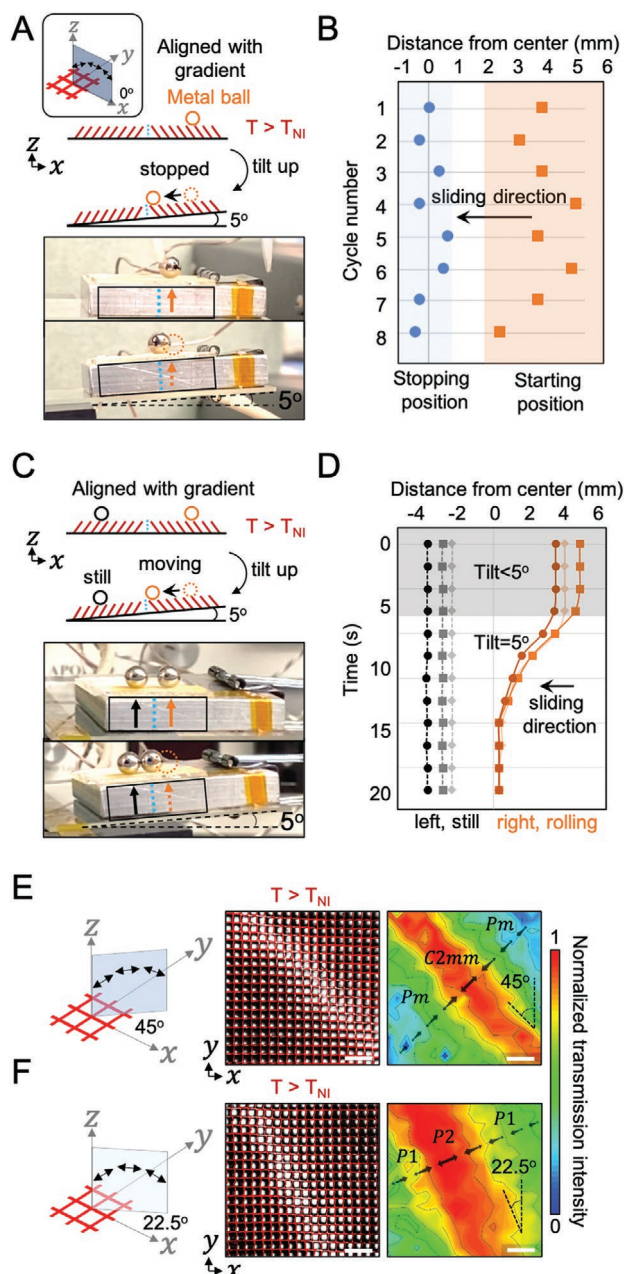


Figure 5. Area-specific symmetry breakings and so-induced material functions. A,B) Controlled object transport for a square lattice with mesogenic director gradually changing from $\gamma = 70^\circ$ to 110° , while keeping $\alpha = 0^\circ$. A) At $T = 135^\circ\text{C} > T_{NI}$, a metal ball stops in the middle of the lattice when tilted by 5° . B) Starting and stopping positions of the metal ball recorded during 8 tests. C,D) Selective object transport for a square lattice with mesogenic director gradually changing from $\gamma = 70^\circ$ to 110° , while keeping $\alpha = 0^\circ$. C) When the lattice is tilted by 5° only the ball on the right side moves as it is characterized by a lower coefficient of friction. D) Trajectories of three pairs of metal balls initially placed at opposite ends of the samples, followed by a tilting to 5° . E,F) Optical microscopy images and transmitted light intensity profile at $T = 135^\circ\text{C} > T_{NI}$ by an LCE square lattice with mesogenic director gradually changing from $\gamma = 70^\circ$ to 110° , while keeping $\alpha = 45^\circ$ (E) or $\alpha = 22.5^\circ$ (F). Double-headed black arrows in the right plots of (E) and (F) denote the projection of the 3D mesogenic director field in the xy -plane. Scale bars: $200\ \mu\text{m}$.

agreement with the results on Figure 4A, a metal ball placed on the LCE lattice slides off at $\theta_{cr} \approx 2^\circ$, when the temperature is increased to $T = 135^\circ\text{C} > T_{NI}$ the ball not only starts sliding at $\theta_{cr} \approx 5^\circ$ (as predicted by the results reported in Figure 4A), but also stops in the middle of the strip, where the shearing direction of the lattices changes abruptly leading to a higher frictional coefficient (Movie S3, Supporting Information). Note that the point of arrest does not depend on the starting positions of the metal ball, confirming the robustness of the controlled object transport (Figure 5B). Finally, our patterned microcellular surface also enables selective object transport. When two identical metal balls were placed on two ends of the sample and the stage was tilted to 5° , only the metal ball on the right side moves and stops at the center, whereas the metal ball on the other side remains still (Figure 5C and Movie S3, Supporting Information). Figure 5D shows the trajectories of three pairs of metal balls and further confirms the robustness of the selectivity over the motion of cargoes placed at different areas of the patterned film. These unique results demonstrate that the combination of transport region control and selective object movement enabled by patterning mechanical deformations and symmetry breakings in LCE cellular structures may lead to applications in the manipulation of object transport on structural surfaces.

The macroscopic patterning of molecular alignment also provides opportunities to realize tunable, area-specific optical modulation. To exemplify this idea, we fabricated an LCE square lattice with mesogenic director gradually changing from $\gamma = 70^\circ$ to 110° , while keeping $\alpha = 45^\circ$ (Figure 5E). As expected, in the nematic phase the lattice transmits light with spatially uniform intensity under optical microscope (Figures S21 and S22, Supporting Information). However, when heated above T_{NI} , the deformed lattice modulates the transmitted light intensity (Figures 5E—middle and right columns, and Figure S22, Supporting Information). In particular, dark-bright-dark regions emerge corresponding to the $Pm-C2mm-Pm$ change of the local symmetry breakings. Moreover, the distribution of transmitted light can be controlled by manipulating the applied magnetic field to vary the nematic directors. As shown in Figure 5F, by changing α from 45° to 22.5° (while keeping the same spatially varying γ), we can re-orient the light band in the isotropic phase at an angle of 22.5° with respect to the vertical direction.

3. Conclusion

We have shown that magnetic field-aligned LCEs provide an excellent platform to program molecular and architectural anisotropy independently and realize reconfigurable cellular structures that exhibit a wide range of temperature-dependent deformation modes, including isotropic/anisotropic buckling, chiral/achiral buckling, tilting, twisting and shearing. These symmetry breakings can be exploited in materials with direction-dependent frictional properties. Furthermore, the unique capabilities of magnetic alignment enables us to encode area-specific molecular anisotropies and the associated localized deformation patterns, of which we showcased potential applications of cellular materials in dynamic light intensity modulation and on-surface object transport. We believe our work not only

unveils general and fundamental materials design principles to further enrich the achievable symmetry breakings and resulting non-trivial deformation modes of cellular structures, but also lays the foundation for the design of the next generation of metamaterials with programmable dynamic direction-dependent properties. Finally, we envision that material fabrication by magnetic alignment can be further combined with other strategies to control the mesogenic director, such as photoalignment and 3D printing, to realize core-shell structures with surface and bulk regions that can be programmed independently.

Supporting Information

Supporting Information is available from the Wiley Online Library or from the author.

Acknowledgements

This work was supported by the National Science Foundation (NSF) through the Designing Materials to Revolutionize and Engineer our Future (DMREF) program under Award No. DMR-1922321 and the Harvard University Materials Research Science and Engineering Center (MRSEC) under Award No. DMR-2011754. K.B. also acknowledges support from the Simons Collaboration on Extreme Wave Phenomena Based on Symmetries. Microfabrication and scanning electron microscopy were performed at the Center for Nanoscale Systems (CNS) at Harvard, a member of the National Nanotechnology Coordinated Infrastructure Network (NNCI), which is supported by the NSF under NSF ECCS Award No. 1541959. The authors would like to thank Bolei Deng, Dr. Michael M. Lerch, Anqi Chen, Dr. Mikhail Zhernenkov, and Dr. Guillaume Freychet for fruitful discussions and experimental help. This research used the SMI beamline (12-ID) of the National Synchrotron Light Source II, a U.S. Department of Energy (DOE) Office of Science User Facility operated for the DOE Office of Science by Brookhaven National Laboratory under Contract No. DE-SC0012704.

Note: The acknowledgements text was updated on October 21, 2021, after initial publication online.

Conflict of Interest

The authors declare no conflict of interest.

Author Contributions

S.L., G.L., and Y.Y. contributed equally to this work. S.L., G.L., Y.Y., J.A., and K.B. conceived the idea and designed the study. G.L. performed the finite element simulations. S.L., Y.Y., A.R., and A.S.Y. performed the experiments. S.L., G.L., Y.Y., J.A., and K.B. analyzed the results and wrote the manuscript with inputs from all authors. J.A., and K.B. supervised the project.

Data Availability Statement

The data that support the findings of this study are openly available at <https://github.com/glibrandi/Liquid-Crystal-Elastomers.git>.

Keywords

cellular microstructures, liquid crystalline elastomers, symmetry breakings

Received: June 30, 2021
Published online: September 2, 2021

- [1] L. J. Gibson, M. F. Ashby, in *Cellular solids: Structure and Properties*, 2nd ed., Cambridge Solid State Science Series, Cambridge University Press, Cambridge, UK **1997**, pp. i–vi.
- [2] R. S. Lakes, *Annu. Rev. Mater. Res.* **2017**, *47*, 63.
- [3] J. Liu, T. Gu, S. Shan, S. H. Kang, J. Weaver, K. Bertoldi, *Adv. Mater.* **2016**.
- [4] J. Valentine, S. Zhang, T. Zentgraf, E. Ulin-Avila, D. A. Genov, G. Bartal, X. Zhang, *Nature* **2008**, *455*, 376.
- [5] H. He, C. Qiu, L. Ye, X. Cai, X. Fan, M. Ke, F. Zhang, Z. Liu, *Nature* **2018**, *560*, 61.
- [6] J. Bauer, S. Hengsbach, I. Tesari, R. Schwaiger, O. Kraft, *Proc. Natl. Acad. Sci. USA* **2014**, *111*, 2453.
- [7] Z. Hu, K. V. Thiyagarajan, A. Bhusal, T. Letcher, Q. Fan, Q. Liu, D. Salem, *Compos. B Eng.* **2017**, *121*, 108.
- [8] J. Summers, *Mater. Des.* **2011**, *32*, 512.
- [9] T. A. Schaedler, A. J. Jacobsen, A. Torrents, A. E. Sorensen, J. Lian, J. R. Greer, L. Valdevit, W. B. Carter, *Science* **2011**, *334*, 962.
- [10] J.-H. Lee, L. Wang, M. C. Boyce, E. L. Thomas, *Nano Lett.* **2012**, *12*, 4392, PMID: 22783965.
- [11] X. Xia, A. Afshar, H. Yang, C. Portela, D. Kochmann, C. Leo, J. Greer, *Nature* **2019**, *573*, 205.
- [12] J. W. Boley, W. M. van Rees, C. Lissandrello, M. N. Horenstein, R. L. Truby, A. Kotikian, J. A. Lewis, L. Mahadevan, *Proc. Natl. Acad. Sci. USA* **2019**, *116*, 20856.
- [13] S. H. Kang, S. Shan, W. L. Noorduin, M. Khan, J. Aizenberg, K. Bertoldi, *Adv. Mater.* **2013**, *25*, 3380.
- [14] Y. Kim, H. Yuk, R. Zhao, S. Chester, X. Zhao, *Nature* **2018**, *558*, 274.
- [15] X. Zhu, Y. Zhang, D. Chandra, S.-C. Cheng, J. M. Kikkawa, S. Yang, *Appl. Phys. Lett.* **2008**, *93*, 161911.
- [16] N. Li, E. Xu, Z. Liu, X. Wang, L. Liu, *Sci. Rep.* **2016**, *6*, 1.
- [17] N. Anantharaju, M. V. Panchagnula, S. Vedantam, S. Neti, S. Tatic-Lucic, *Langmuir* **2007**, *23*, 11673.
- [18] J. Shim, P. Wang, K. Bertoldi, *Int. J. Solids Struct.* **2015**, *58*, 52.
- [19] T. J. White, D. J. Broer, *Nature Mater.* **2015**, *14*, 1087.
- [20] C. Ohm, M. Brehmer, R. Zentel, *Adv. Mater.* **2010**, *22*, 3366.
- [21] M. Yamada, M. Kondo, J.-i. Mamiya, Y. Yu, M. Kinoshita, C. J. Barrett, T. Ikeda, *Angew. Chem., Int. Ed.* **2008**, *47*, 4986.
- [22] K. Urayama, S. Honda, T. Takigawa, *Macromolecules* **2006**, *39*, 1943.
- [23] A. Kaiser, M. Winkler, S. Krause, H. Finkelmann, A. M. Schmidt, *J. Mater. Chem.* **2009**, *19*, 538.
- [24] J. Shin, M. Kang, T. Tsai, C. Leal, P. V. Braun, D. G. Cahill, *ACS Macro Lett.* **2016**, *5*, 955.
- [25] T. H. Ware, M. E. McConney, J. J. Wie, V. P. Tondiglia, T. J. White, *Science* **2015**, *347*, 982.
- [26] J.-a. Lv, Y. Liu, J. Wei, E. Chen, L. Qin, Y. Yu, *Nature* **2016**, *537*, 179.
- [27] H. Aharoni, Y. Xia, X. Zhang, R. D. Kamien, S. Yang, *Proc. Natl. Acad. Sci. USA* **2018**, *115*, 7206.
- [28] Y. Guo, H. Shahsavan, M. Sitti, *Adv. Mater.* **2020**, *32*, 2002753.
- [29] J. Küpfer, H. Finkelmann, *Die Makromol. Chem., Rapid Commun.* **1991**, *12*, 717.
- [30] A. Kotikian, R. L. Truby, J. W. Boley, T. J. White, J. A. Lewis, *Adv. Mater.* **2018**, *30*, 1706164.
- [31] M. López-Valdeolivas, D. Liu, D. J. Broer, C. Sánchez-Somolinos, *Macromol. Rapid Commun.* **2018**, *39*, 1700710.
- [32] A. Buguin, M.-H. Li, P. Silberzan, B. Ladoux, P. Keller, *J. Am. Chem. Soc.* **2006**, *128*, 1088.
- [33] Y. Yao, J. T. Waters, A. V. Shneidman, J. Cui, X. Wang, N. K. Mandsberg, S. Li, A. C. Balazs, J. Aizenberg, *Proc. Natl. Acad. Sci. USA* **2018**, *115*, 12950.
- [34] P.-G. De Gennes, J. Prost, *The Physics of Liquid Crystals*, vol. 83, Oxford University Press, Oxford, UK **1993**.
- [35] M. T. Sims, L. C. Abbott, R. M. Richardson, J. W. Goodby, J. N. Moore, *Liq. Cryst.* **2019**, *46*, 11.
- [36] Z. L. Wu, A. Buguin, H. Yang, J.-M. Taulemesse, N. Le Moigne, A. Bergeret, X. Wang, P. Keller, *Adv. Funct. Mater.* **2013**, *23*, 3070.
- [37] A. H. Gelebart, D. J. Mulder, M. Varga, A. Konya, G. Vantomme, E. W. Meijer, R. L. B. Selinger, D. J. Broer, *Nature* **2017**, *546*, 632.
- [38] D. L. Thomsen, P. Keller, J. Naciri, R. Pink, H. Jeon, D. Shenoy, B. R. Ratna, *Macromolecules* **2001**, *34*, 5868.
- [39] P. H. Butler, *Point Group Symmetry Applications: Methods and Tables*, Springer Science & Business Media, New York **2012**.